

Maximum Production Point Tracking of a High-Temperature Power-to-Gas System: A Dynamic-Model-Based Study

Xuetao Xing, *Student Member, IEEE*, Jin Lin, *Member, IEEE*, Yonghua Song, *Fellow, IEEE*, Qiang Hu

Abstract—Power-to-gas (P2G) can be employed to balance renewable generation because of its feasibility to operate at fluctuating loading power. The fluctuating operation of low-temperature P2G loads can be achieved by controlling the electrolysis current alone. However, this method does not apply to high-temperature P2G (HT-P2G) technology with auxiliary parameters such as temperature and feed rates: Such parameters need simultaneous coordination with current due to their great impact on conversion efficiency. To improve the system performance of HT-P2G while tracking the dynamic power input, this paper proposes a maximum production point tracking (MPPT) strategy and coordinates the current, temperature and feed rates together. In addition, a comprehensive dynamic model of an HT-P2G plant is established to test the performance of the proposed MPPT strategy, which is absent in previous studies that focused on steady states. The case study suggests that the MPPT operation responds to the external load command rapidly even though the internal transition and stabilization cost a few minutes. Moreover, the conversion efficiency and available loading capacity are both improved, which is definitely beneficial in the long run.

Index Terms—High-temperature power-to-gas, maximum production point tracking, dynamic loading power.

NOMENCLATURE

A. Constants and Variables

F	Faraday constant.
M	Molar mass.
T, p	Temperature, pressure.
c, C	Specific heat capacity, heat capacity (isobaric).
U	Voltage or overvoltage.
I, i	Current, current density.
w	Mass flow rate of the gas mixture.
π	Feed factor.
P, Q	Active power, reactive power.
η	Efficiency.
τ	Time constant.
N	Number.
R, C, Φ	Resistance, capacitance, flux linkage.
J, Ω	Angular mass, angular velocity.
s	Laplace variable.

Xuetao Xing and Jin Lin are with the State Key Laboratory of Control and Simulation of Power Systems and Generation Equipment, Department of Electrical Engineering, Tsinghua University, Beijing 100084, China (e-mail: linjin@tsinghua.edu.cn).

Yonghua Song is with the Department of Electrical and Computer Engineering, University of Macau, Macau, China, and with the Department of Electrical Engineering, Tsinghua University, Beijing 100084, China.

Qiang Hu is with Tsinghua-Sichuan Energy Internet Research Institute, Chengdu 610213, China.

k, K Dimensionless coefficient, PID parameter.
 p, w, π $[p_{\text{H}_2\text{O}} \ p_{\text{H}_2} \ p_{\text{O}_2}]^T, [w_{\text{ca}} \ w_{\text{an}}]^T, [\pi_{\text{ca}} \ \pi_{\text{an}}]^T$.

B. Subscripts

ca, an, el	Cathode, anode, electrolysis.
rev, th	Reversible, thermo-neutral (voltage).
act, con, ohm	Activation, concentration, ohmic (overvoltage).
war, rea, rec	Warming, reaction, heat recovery.
pre, fur, cel	Preheater, furnace, (SOC) cell.
pum, com, cvt	Pump, compressor, converter.
flt, nom, gen	Filter, nominal, generate.
mot, fra	Motor, fraction.
vap, liq, amb	Vaporization, liquid, ambient.
thr, opt, ref	Threshold, optimal, reference.
in, out	Inlet, outlet position of the furnace.
p, i, d	Proportion, integration, differentiation.

I. INTRODUCTION

THE penetration and utilization ratios of renewable generation sources are limited by the adverse grid-side impacts of their naturally intermittent outputs. In this context, the emerging technology of power-to-gas (P2G) provides the necessary flexibility to complement source-side uncontrollability and thus facilitate renewable integration [1].

The idea is that P2G can operate at various loading conditions and that the coupling gas demands (injected into storage tanks or directly into gas pipelines) are typically flexible [2], [3]. Therefore, the loading power of P2G can rapidly track the fluctuating dispatch commands, which can be generated by the grid regulator to moderate the peak power and balance the uncontrollable renewable energy [4], [5]. In this manner, the renewable energy that may otherwise be curtailed can be used to produce easily applicable fuel gases. Several pilot projects of P2G participating renewable energy regulation have been realized worldwide [3], [6].

For commercialized low-temperature P2G technologies (typically below 100°C [6]), the system loading power is almost totally attributed to the electric energy consumed by the electrolysis process, where H₂O splits into H₂ and O₂. By altering the electrolysis current with a necessary power converter, the loading power can respond to the command signal rapidly, which has been verified to be fast enough to participate in automatic generation control (AGC) [7].

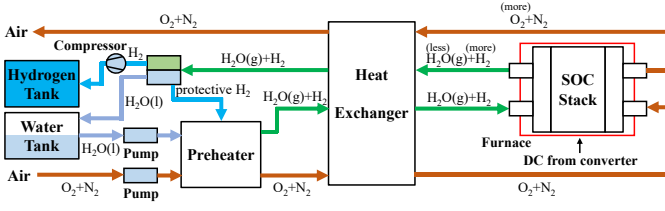


Fig. 1. General structure of an HT-P2G system [4], [9].

High-temperature P2G (HT-P2G) is a developing technology that employs solid oxide cells (SOCs) to electrolyze vaporous water, as shown in Fig. 1. Auxiliary modules such as the preheater, the heat exchanger and the furnace are typically required for necessary heating. Relative to traditional low-temperature P2G technologies, HT-P2G can achieve higher conversion efficiency because the electrolysis reaction is facilitated both thermodynamically and kinetically at elevated temperatures (typically above 750°C) [8]. Nevertheless, the traditional current-controlled-alone method of low-temperature P2G is not well suited to HT-P2G: Despite the fact that the controlling current is sufficient for tracking the desired loading power [2], [4], [8], the system performance of HT-P2G is far from optimal without the simultaneous coordination of other HT-P2G parameters such as stack temperature and feed flow rates [2], which affects the power consumption of auxiliary modules and thus the conversion efficiency. This topic is the focus of this paper.

The fundamentals of HT-P2G operation, such as models of SOCs and auxiliary modules, have long been described in the literature. Reference [8] presented a one-dimensional SOC model to evaluate the cell voltage from the electrolysis current with a reversible voltage and various overvoltages, which was validated experimentally in [10]. Reference [11] built a lumped model with transfer functions to succinctly describe the electrical dynamics of an SOC stack. As for models of necessary auxiliaries including the power converter, furnace (or heater), pump and compressor, such information can also be found in the literature [2], [12], [13].

Based on the above fundamental studies, research papers have discussed the parameter optimization of a running HT-P2G system. Reference [14] analyzed the correlation between the overall H_2 production efficiency and the operating parameters, such as the temperature, production rate, steam utilization and air sweep, based on a simulated HT-P2G system coupled to a nuclear reactor. Reference [4] focused on the impacts of the H_2 recirculation rate and steam utilization on the system efficiency of a reversible SOC plant. Reference [15] calculated the optimal HT-P2G operating points at various loading conditions using a multi-objective optimizer and conducted further analysis with the obtained scatter diagrams. Reference [16] performed a simulation-based investigation of the energy efficiency and its dependence on feedstock composition, cathode feed rate, temperature, SOC pressure, among other parameters. As a result of these HT-P2G optimization studies, some principles to achieve higher system performance have been commonly accepted, such as reducing the air sweep and enhancing the steam utilization. Neverthe-

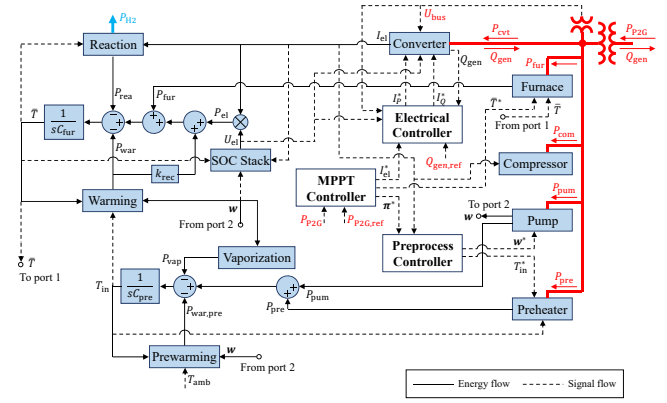


Fig. 2. Overall dynamic model of an HT-P2G system (the involved submodels are elaborated in Fig. 3, Fig. 4 and Fig. 5; the controller designs are presented in Fig. 7 and Fig. 8).

less, these studies mostly focused only on the improvement of steady-state performance, while the investigation of dynamic models has not been presented. In other words, the research to describe the plant's transient behaviors considering inherent inertia is currently insufficient, which is essentially required in developing advanced control strategies to track fluctuating load commands.

In this paper, the optimization of operating parameters is combined with a comprehensive dynamic model of an HT-P2G system that describes its transient behaviors. Specifically, a maximum production point tracking (MPPT) control strategy is proposed to enable the HT-P2G plant to rapidly track the desired loading power profile and simultaneously maximize the steady-state energy conversion efficiency by coordinating various auxiliary modules properly. The effects of the proposed strategy are validated with a practical case where an HT-P2G plant is dispatched to implement AGC as a flexible load.

This paper primarily achieves the following contributions: 1) An integrated HT-P2G dynamic model is presented to describe a system's dependence on temperature and feed flow parameters considering auxiliary but necessary energy consumptions and to depict its transient behaviors with multi-scale dynamics of several coupled domains (such as the electrical domain, thermodynamics and hydromechanics); 2) An MPPT control strategy is proposed to coordinate the temperature and feed flow parameters other than electrolysis current, which shows a fast response speed to track the loading power command in the short term and significantly beneficial effects by increasing the production efficiency and available capacity in the long run.

II. DYNAMIC DESCRIPTION OF AN HT-P2G SYSTEM

A. Overall Model of the System

As shown in Fig. 1, a typical HT-P2G system consists of an SOC stack where water electrolysis occurs in addition to necessary auxiliary modules such as converter, preheater, pump group, furnace and compressor [2], [4], [15], [17]. Driven by the pump group, H_2O (mass flow rate w_{ca} , with some protective H_2 [4], [8]) and sweep air (mass flow rate w_{an}) first goes through the preheater that vaporizes water and

then enters the furnace, where steam and air are further heated and fed into the cathode channels and anode channels of the SOC stack, respectively. Inside each SOC, steam is converted into H_2 at average SOC temperature \bar{T} with the presence of DC electrolysis current I_{el} provided by the converter. After leaving the furnace, the H_2 -rich humid gas is condensed for purification and then pressurized to p_{com} by the compressor as the final product.

The whole system model of Fig. 1 is shown in Fig. 2. The SOC productive condition (I_{el}, \bar{T}, w) is ensured by the controlled auxiliary modules, whose energy consumptions add up to the system loading power P_{P2G} . In addition, the energy balances regarding the heating processes within furnace and preheater are modeled to evaluate the variations of \bar{T} and T_{in} , respectively. Note that the solid blocks in Fig. 2 represent inherent elements or physical relations, while the hollow blocks represent artificially designed controllers. We provide a closer view of this model in the following subsections.

B. Dynamic Models of the Energy Balances

According to [2], the furnace volume energy balance can be described as

$$C_{fur} \frac{d\bar{T}}{dt} \doteq U_{el} I_{el} + P_{fur} + k_{rec} P_{war} - P_{war} - P_{rea}. \quad (1)$$

The energy used for feedstock warming (P_{war}) and the electrolysis reaction (P_{rea}) is subtracted from the energy provided by the furnace (P_{fur}), DC current ($U_{el} I_{el}$) and heat recovery ($k_{rec} P_{war}$) to obtain the net input energy, which accounts for the change in \bar{T} . Here, k_{rec} is the heat recovery coefficient, representing the fraction of exhaust heat recovered for inlet gas warming. In the preprocess, the energy is primarily distributed to warming ($P_{war,pre}$) and vaporization (P_{vap}), and the energy balance can be analogously formulated as

$$C_{pre} \frac{dT_{in}}{dt} \doteq P_{pre} + P_{pum} - P_{war,pre} - P_{vap}. \quad (2)$$

Note that C_{fur} and C_{pre} are equivalent heat capacities that can be measured experimentally.

Relations (1) and (2) are included in Fig. 2, and detailed models of the aforementioned energy sinks are depicted in Fig. 3. Note that P_{war} and $P_{war,pre}$ are calculated from the corresponding heat capacities and temperature increments, while P_{rea} and P_{vap} are calculated from the enthalpy changes in the electrolysis or vaporization process.

C. Dynamic Model of the SOC Stack

According to [11], the SOC stack can be modeled as shown in Fig. 4. This model outputs the dynamic behavior of stack voltage U_{el} based on I_{el} , \bar{T} and the feedstock flow rates w_{ca} and w_{an} . The cell voltage $U_{cel}(i_{el}, \bar{T}, \bar{p})$ is calculated by totaling the reversible voltage (U_{rev}) and various overvoltages (U_{ohm} , U_{act} and U_{con}). The average partial pressures p_{H_2O} , p_{H_2} and p_{O_2} are determined by the feed factors π_{ca} and π_{an} , which represent the ratios of actual provided H_2O and O_2 to their reaction-correlated quantities in the channels of cathode and anode, respectively. (Alternatively, some papers use the steam conversion rate and air ratio, which are actually $\frac{1}{\pi_{ca}}$

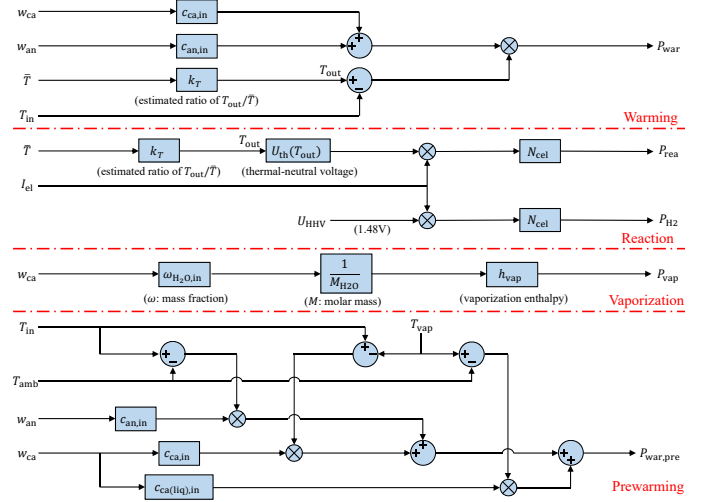


Fig. 3. Dynamic models of primary energy sinks (based on [2]).

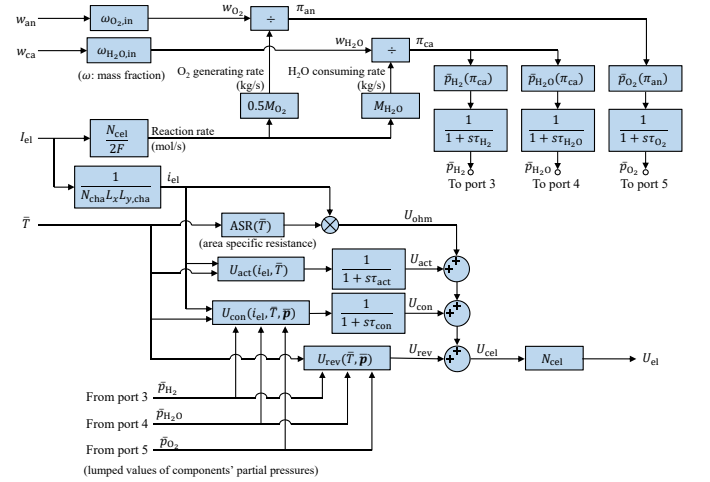


Fig. 4. Dynamic model of the SOC stack (based on [11], [18] and [19]).

and π_{an} , respectively [2].) Note that the first-order delays of τ_{act} and τ_{con} arise from the cell's electrochemical double-layer phenomenon [18] and that the pressure inertia described by τ_{H_2O} , τ_{H_2} and τ_{O_2} arises from the finite gas flow rates [11], [19]. Note that the model of Fig. 4 is reversible: its output can still describe the SOC stack voltage when $I_{el} < 0$ (fuel cell mode); only the overvoltages U_{ohm} , U_{act} and U_{con} are negative values.

D. Dynamic Models of the Auxiliary Modules

The primary auxiliary modules of HT-P2G can be modeled as Fig. 5. Below is a detailed explanation.

1) *Converter*: According to [20], a three-phase PWM converter is preferred for medium- and high-power SOC applications, owing to its simple control and bidirectional power flow. Here, we simply employ a first-order delay of τ_{cvt} to model the rapid control of active and reactive components of the grid-side current, I_P and I_Q , which can be realized with classic decoupled dq -current control loops and the phase-locked loop of grid voltage [23], [24]. Then, the converter's reactive output

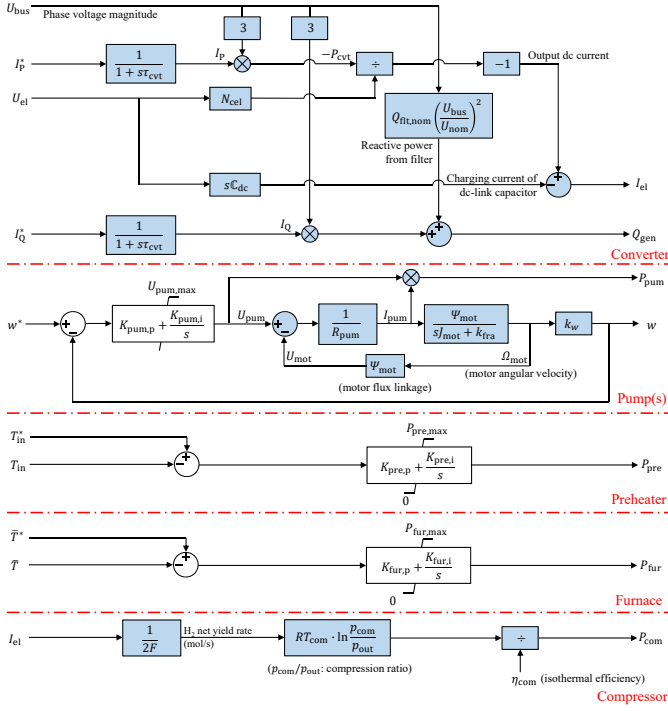


Fig. 5. Dynamic models of various auxiliary modules (based on [20], [12], [21] and [22]).

Q_{gen} , including the reactive generation of the filter, can be derived from I_Q . On the DC side, the electrolysis current I_{el} can be obtained by extracting the charging current of the DC link capacitor C_{dc} from the total DC current derived from I_P .

2) *Pump*: The DC-motor-based model in [12] is employed to describe the metering pumps that drive the feedstock flows in both the cathode and anode channels. As shown in Fig. 5, the flow rate w_{ca} (or w_{an}) is controlled by a built-in fast current controller.

3) *Preheater and Furnace*: Employing the convectional design of heaters [21], the preheater and the furnace are regarded as electric heaters with built-in PI controllers to track the desired T_{in} and \bar{T} , respectively, as shown in Fig. 5.

4) *Compressor*: According to [22], the compressor's energy consumption P_{com} can be modeled by multiplying the molar flow of the output H_2 and the logarithm of the compression ratio $\ln \frac{P_{\text{com}}}{P_{\text{out}}}$, considering its isothermal efficiency η_{com} .

III. MAXIMUM PRODUCTION POINT TRACKING

A. Maximum Production Point (MPP) Solver

A comprehensive steady-state model of the HT-P2G system is required to find its maximum production point (MPP) where the conversion efficiency η_{P2G} is optimized. First, the total energy consumption should meet the desired loading power $P_{\text{P2G,ref}}$:

$$\underline{U}_{\text{el}} I_{\text{el}} + P_{\text{fur}} + P_{\text{pre}} + P_{\text{pump}} + \underline{P}_{\text{com}} = P_{\text{P2G,ref}} \quad (3)$$

Furthermore, the steady-state equations of (1) and (2) should be fulfilled:

$$\underline{U}_{\text{el}} I_{\text{el}} + P_{\text{fur}} + k_{\text{rec}} \underline{P}_{\text{war}} - \underline{P}_{\text{war}} - \underline{P}_{\text{rea}} = 0 \quad (4)$$

$$P_{\text{pre}} + P_{\text{pump}} - \underline{P}_{\text{war,pre}} - \underline{P}_{\text{vap}} = 0 \quad (5)$$

In addition, for steady operating states, there exists a maximum electrolysis current $I'_{\text{el,max}}$ at given P_{fur} and π to ensure that the feedstock is not excessive and thus can be heated up to at least the lowest electrolysis temperature T_{min} at the stack entrance. In other words, $I'_{\text{el,max}}$, which represents the maximum feeding rate affordable by the current furnace power, can be obtained from the measured steady-state I_{el} when the stack entrance temperature just reaches T_{min} .

$$I_{\text{el}} \leq I'_{\text{el,max}}(P_{\text{fur}}, \pi) \quad (6)$$

Additionally, the primary parameters have upper and lower limits to ensure the safe operation of the SOC stack:

$$T_{\text{min}} \leq \bar{T} \leq T_{\text{max}} \quad (7)$$

$$I_{\text{el,min}} \leq I_{\text{el}} \leq I_{\text{el,max}} \quad (8)$$

$$\pi_{\text{ca}} > 1, \pi_{\text{an}} \geq 0 \quad (9)$$

Then, the MPP can be acquired by maximizing η_{P2G} :

$$\max_{I_{\text{el}}, \bar{T}, \pi} \frac{N_{\text{cel}} I_{\text{el}} U_{\text{HHV}}}{P_{\text{P2G,ref}}} \quad (10)$$

within the constraints of (3)-(9). Note that the aforementioned underlined variables $\underline{U}_{\text{el}}$, $\underline{P}_{\text{con}}$, $\underline{P}_{\text{com}}$, $\underline{P}_{\text{war}}$, $\underline{P}_{\text{war,pre}}$, $\underline{P}_{\text{rea}}$ and $\underline{P}_{\text{vap}}$ can all be simply derived from the operating parameters $(I_{\text{el}}, \bar{T}, \pi)$ based on the steady states of the dynamic models described in Section II-B, II-C and II-D, as elaborated in Appendix A. By employing the interior-point algorithm, (3)-(10) are sufficient for solving MPPs numerically at various loading conditions $P_{\text{P2G,ref}}$.

B. Visualized Explanations of MPP Locating

Based on the numerical MPP solutions obtained in Section III-A, patterns can be found to help us understand the MPP problem in a visual manner:

1) π_{an} is always zero (i.e., no sweep air) at MPPs. A larger π_{an} (i.e., a large sweep air flow rate) increases the required energy for heating but also benefits the system by lowering \bar{p}_{O_2} , $\underline{U}_{\text{el}}$ and thus the required energy for the converter. However, the drop in $\underline{U}_{\text{el}}$ due to π_{an} is essentially negligible because the oxygen fraction is included as a logarithm when calculating $\underline{U}_{\text{el}}$; it ranges (0.21, 1] but never approaches zero when π_{an} rises. In this context, the sweep air does not detectably benefit the system performance, which is consistent with the analyses in [4] and [14].

2) I_{el} is always kept at $I'_{\text{el,max}}$ at MPPs. In other words, the constraint (6) is always active at optimal solutions, and the furnace power P_{fur} is used at its fullest. If not, one can always lower the parameter \bar{T} or π_{ca} (but maintain I_{el}) appropriately to reduce actual P_{fur} and then fulfill the equality sign of (6); the new steady state has a lowered P_{P2G} and thus a higher η_{P2G} . We designate (6) as the ‘‘furnace constraint’’ (FC) for convenience.

Based on the two patterns above, we can understand the MPP problem (3)-(10) as ‘‘finding the optimal \bar{T} and π_{ca} that maximize $I_{\text{el}}(\bar{T}, \pi_{\text{ca}})$ on the FC curve’’. Here, π_{an} is kept at zero, and $I_{\text{el}}(\bar{T}, \pi_{\text{ca}})$ can be explicitly obtained from (3)-(5).

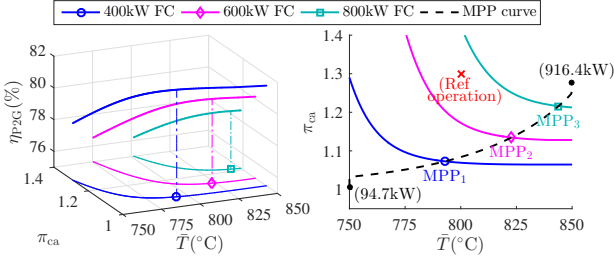


Fig. 6. Solving the optimal operating states at various $P_{P2G,ref}$ to obtain the MPP curve.

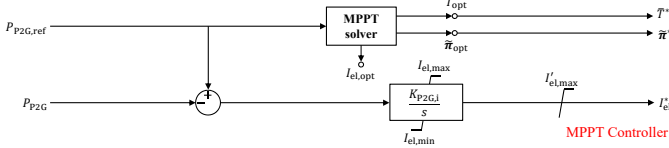


Fig. 7. Design of the MPPT controllers.

For the subsequent numerical case of Section IV, the MPP location process is depicted in the left-hand plot of Fig. 6. Then, the MPP curve can be obtained from the locus of MPPs at various loading conditions (value of $P_{P2G,ref}$), such as MPP₁ at 300kW, MPP₂ at 600kW, MPP₃ at 800kW, and so on, as shown in the right-hand plot of Fig. 6. For a given HT-P2G system, the numerical MPP curve can be calculated in advance and stored in the MPP solver so that a look-up table can be provided during practical real-time control to reduce the computational cost. The computed optimal parameters ($I_{el,opt}$, \bar{T}_{opt} , π_{opt}) play important roles in the whole MPPT control strategy, as shown in Fig. 7.

C. MPPT Controller

As shown in Fig. 2, the MPPT controller computes the operating parameter commands \bar{T}^* , π^* and I_{el}^* from the actual and reference loading power P_{P2G} and $P_{P2G,ref}$. The proposed design of the MPPT controller to ensure both a rapid tracking response and an improved steady-state efficiency is illustrated in Fig. 7. The aforementioned MPP solver is implemented here to calculate the optimal parameters ($I_{el,opt}$, \bar{T}_{opt} , π_{opt}), while only \bar{T}_{opt} and π_{opt} are employed as \bar{T}^* and π^* , respectively. On the other hand, the current command I_{el}^* is calculated by integrating the tracking error between P_{P2G} and $P_{P2G,ref}$. The upper limit $I_{el,max}'$ in (6) is activated when P_{fur} stabilizes at a nonzero value.

In this way, the fast dynamics of power converter can be used to eliminate—in a timely manner—the tracking error of the loading power, when the furnace and pumps are gradually responding to their altered set points. In other words, the MPPT controller takes advantage of the fast current control to complement the slow responses of the temperature and flow rates, ensuring the system's dynamic performance. In addition, an optimized steady-state system performance is achieved as a result of the updated set points from MPP solver. Note that the electrolysis current I_{el} ultimately automatically stabilizes at $I_{el,opt}$ because the system steady state is uniquely determined by \bar{T} , π and $P_{P2G,ref}$ according to (3)-(6).

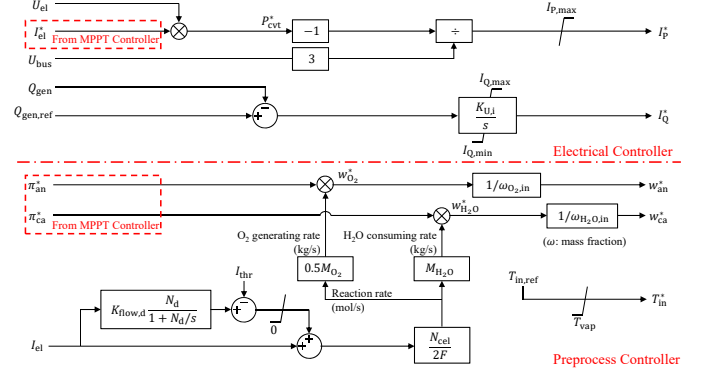


Fig. 8. Design of the electrical controller and the preprocess controller.

The computed \bar{T}^* is implemented by the internal PI controller of furnace as shown in Fig. 5, but I_{el}^* and π^* need to be further processed in the following electrical controller and preprocess controller, as shown in Fig. 8.

D. Electrical Controller

The commands of the active and reactive grid-side current for the power converter, I_P^* and I_Q^* , are computed by the electrical controller, whose design is presented in Fig. 8. This design is modified from the electrical control module of a full converter wind turbine generator [24]. To provide the appropriate active power requested for electrolysis, I_P^* is calculated from the electrolysis current order I_{el}^* provided by the aforementioned MPPT controller based on the AC-DC active power balance. On the other hand, the reactive power reference $Q_{gen,ref}$ is compared to the actual reactive power generation Q_{gen} , and the resulting error is integrated to generate I_Q^* .

The computed I_P^* and I_Q^* are implemented by the aforementioned dq -current control loops and phase-locked loop of the power converter, which are represented as first-order delays of τ_{cvt} in Fig. 5 of Section II-D.

E. Preprocess Controller

As shown in Fig. 2 and Fig. 8, the preprocess controller monitors the commands of feed factors π_{ca}^* and π_{an}^* given by the MPPT controller and restores the commands of the feed flow rates w_{ca}^* and w_{an}^* from them. The actual electrolysis current I_{el} is required for computing the reaction rate used in the restoration. The computed w_{ca}^* and w_{an}^* are implemented by the internal PI controllers of metering pumps of Section II-D, as shown in Fig. 5.

However, if we employ the current value of I_{el} as the multiplier directly, feedstock starvation that damages the stack will probably occur when I_{el} meets a sharp rise. Although w_{ca}^* and w_{an}^* follow the change, the actual flow rates w_{ca} and w_{an} cannot rise immediately due to the inertia of the pumps, resulting in an undesired drop of the actual feed factors π_{ca} and π_{an} and thus starvation. Therefore, a differential block ($\frac{N_d}{s+N_d}$ to reduce the controller's sensitivity to noise [25]) is employed in Fig. 8 to compute a correction of I_{el} based on the changing rate.

TABLE I
PRIMARY MODEL PARAMETERS OF THE NUMERICAL HT-P2G SYSTEM

Parameters	Values	Units	Parameters	Values	Units
$I_{el,min}$	53.3	A	$I_{el,max}$	480.0	A
T_{min}	750	$^{\circ}\text{C}$	T_{max}	850	$^{\circ}\text{C}$
k_{rec}	20%	1	k_T	1.085	1
τ_{H_2}	2.61	s	τ_{H_2O}	3.92	s
τ_{O_2}	2.91	s	τ_{act}	0.23	s
τ_{con}	0.23	s	τ_{cvt}	0.02	s

If the correction is larger than a specific threshold value I_{thr} (signifying a sharp rise in I_{el}), this correction is incorporated into the current value of I_{el} to compute I'_{el} , which can be regarded as the predicted value of I_{el} for $K_{flow,d}$ seconds later. This design of the preprocess controller ensures the early action of pumps to provide sufficient and timely feed flow rates w_{ca} and w_{an} .

Additionally, the preprocess controller provides the temperature command for the preheater, T_{in}^* , which is typically set as a constant higher than T_{vap} to ensure the vaporization of water.

IV. CASE STUDY

In this section, an intact HT-P2G system with a 1000-cell SOC stack is numerically modeled in the manner of Fig. 2 to validate the effects of the proposed MPPT strategy. First, the transient process between steady states is analyzed in Section IV-B as Scenarios A and B to observe the short-term response performance in tracking the load command. Then, the system operation under a fluctuating power input is investigated in Section IV-C as Scenario C to reveal the long-term production benefits.

A. Case Settings

The modeled HT-P2G system is based on the cell parameters in [8], the dynamic parameters in [11], [18] and [24], and the necessary physical properties of involved gases. The primary model parameters are listed in Table I, and the inlet compositions are $H_2O(90\text{vol.}\%) + H_2(10\text{vol.}\%)$ at the cathode and $O_2(21\text{vol.}\%) + N_2(79\text{vol.}\%)$ at the anode. Matlab-Simulink is employed to implement the model and run dynamic simulations.

The example model is simulated as a single plant connected to an infinite bus to study its dynamic response when a variation of the load command $P_{P2G,ref}$ is imposed. The bus voltage U_{bus} and the plant's power factor are kept at the rated values (12.66kV) and 0.9, respectively, and $P_{P2G,ref}$ is the only varying external variable.

The MPPT operation calculates the optimal temperature and feed flow rates to the control furnace and pumps that maximize the conversion efficiency according to the temporal load command $P_{P2G,ref}$, as depicted by (3)-(10) and the MPP curve in Fig.6. For comparison, a reference operation strategy is employed as a benchmark, which sets the temperature and feed flow rates at fixed values ($T^* \equiv 800^{\circ}\text{C}$, $\pi_{ca}^* \equiv 1.3$

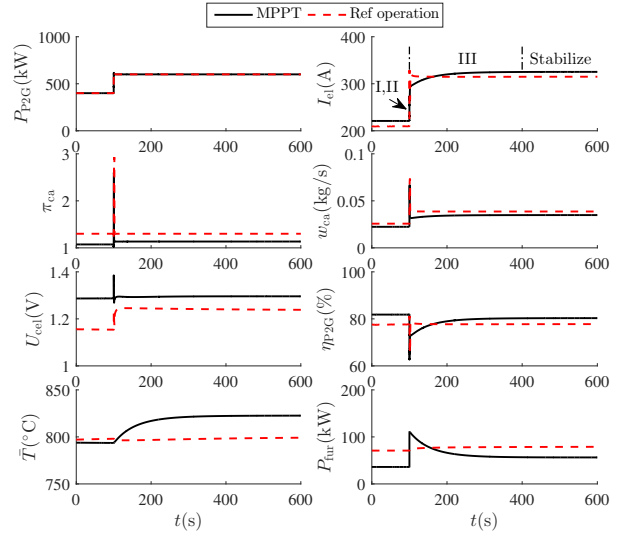


Fig. 9. The 500-second transient response of the HT-P2G system when $P_{P2G,ref}$ steps from 400kW to 600kW (MPP₁→MPP₂): Scenario A.

and $\pi_{an}^* \equiv 0$ in the MPPT controller of Fig. 7) and only controls the electrolysis current to meet the desired $P_{P2G,ref}$, as depicted by the cross marker in Fig. 6.

B. Transient Process between Steady States

We simulated two transition scenarios for the modeled HT-P2G system. In Scenario A, the load command $P_{P2G,ref}$ of the modeled HT-P2G system steps from 400kW to 600kW at $t = 100\text{s}$, which actually represents the transient process from MPP₁ to MPP₂ in the steady-state plot of Fig. 6. In Scenario B, $P_{P2G,ref}$ of the modeled HT-P2G system steps from 400kW to 800kW at $t = 100\text{s}$. The resultant transient responses of the primary variables in the subsequent 500s actually represents the transient process from MPP₁ to MPP₃ in Fig. 6. The resultant transient responses of primary variables in the subsequent 500s of Scenario A and B are illustrated in Fig. 9 and Fig. 11, respectively. The first 5-second process immediately after the step of Scenario A is presented in magnified form in Fig. 10. Based on these figures, the following effects of the proposed MPPT strategy can be observed:

1) Rapid Tracking with Improved Efficiency (Scenario A):

As marked in Fig. 9 and Fig. 10, the entire transient process of MPPT operation includes three stages before the system stabilizes at the new steady state MPP₂. In Stage I, the imposed error between $P_{P2G,ref}$ and P_{P2G} causes I_{el} to ramp up sharply as a result of fast current control of the PWM converter. After approximately 0.15s, the actual load P_{P2G} has essentially shifted to the updated $P_{P2G,ref}$, moving into Stage II. In Stage II, the cathode feeding rate w_{ca} is boosted by the metering pump following the prediction control of the preprocess controller for a sharp-current-rise situation, causing simultaneous variation of P_{pre} for preheating and vaporization. As a result of the rapidly controlled I_{el} , the variation of P_{pre} is well compensated, and only small ripples are reflected on P_{P2G} . After approximately 2s, the effects of the boosted w_{ca} pass, and I_{el} achieves a relative stabilization but is still

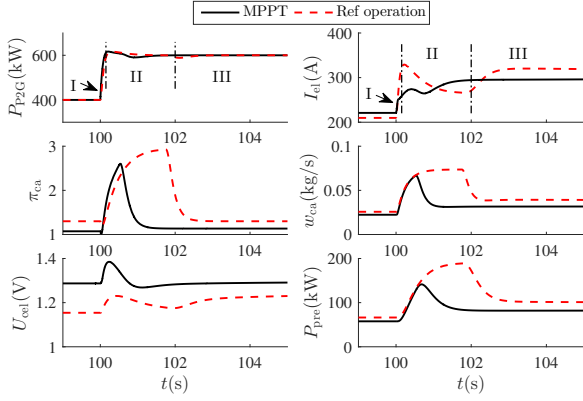


Fig. 10. The 5-second transient response of the HT-P2G system when $P_{P2G,ref}$ steps from 400kW to 600kW (MPP₁→MPP₂): Magnified Scenario A.

TABLE II

THREE STAGES IN THE STEP-UP SYSTEM RESPONSE OF MPPT OPERATION

Stage	Stage I	Stage II	Stage III
Process	P_{P2G} responding	P_{P2G} stabilizing	P_{P2G} stabilizing
Disturbance	Stepped $P_{P2G,ref}$	Varying P_{pre}	Varying P_{fur}
Ripple of P_{P2G}	Abrupt	Small	Almost gone
Time scale	Deciseconds	Seconds	Minutes
Dynamic source	I_{el} (converter)	w_{ca} (pump)	\bar{T} (furnace)

gradually increasing because \bar{T} and P_{fur} are not yet stabilized. In Stage III, \bar{T} slowly shifts towards the optimal temperature at MPP₂, and the decreasing error between \bar{T} and \bar{T}^* causes P_{fur} to decrease simultaneously. I_{el} is controlled accordingly to compensate the decreasing P_{fur} in a much faster speed; thus, ripples of P_{P2G} are generally not found in this stage. After approximately 400s, the whole system is essentially stabilized and ultimately arrives at the new state of MPP₂. The features of these three stages are summarized in Table II.

In contrast, the transient process of reference operation in Fig. 9 and Fig. 10 contains only two stages: Stage I and Stage II. In fact, the division of the three stages of the MPPT transient process is due to the naturally different time constants of I_{el} , w_{ca} and \bar{T} . The reference operation holds a constant temperature as shown in Fig. 6; thus, it is not surprising that Stage III is omitted.

For both operations, the actual load P_{P2G} shifts to the updated $P_{P2G,ref}$ in approximately 0.15s-0.2s (Stage I), followed by small ripples lasting for approximately 2s-3s (Stage II), which indicates satisfactory external performance in terms of dynamic response for grid-side regulation. As for the internal dynamic performance, the MPPT strategy has a much longer transient process than the reference operation due to the presence of Stage III. However, as shown in Fig. 9, the conversion efficiency η_{P2G} under MPPT is always higher than the reference operation at steady state. In other words, more hydrogen is produced by the HT-P2G plant (the production rate is proportional to I_{el}) during long-term MPPT operation. Note that the short-lived valley of η_{P2G} is due to the temporal demand of power accumulation while shifting towards an

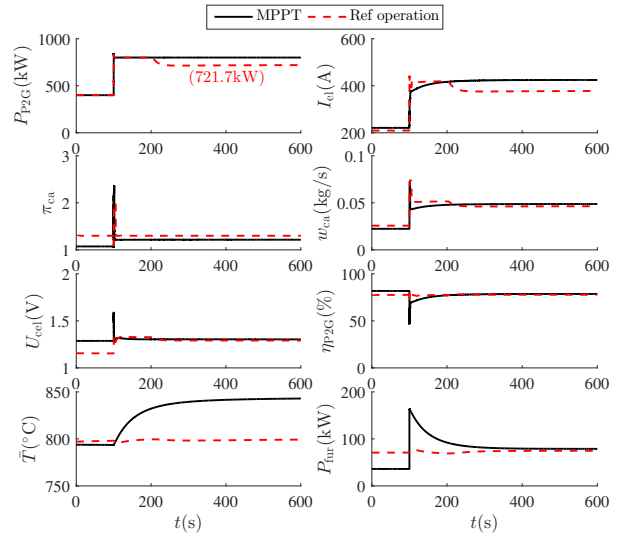


Fig. 11. The 500-second transient response of the HT-P2G system when $P_{P2G,ref}$ steps from 400kW to 800kW (MPP₁→MPP₃): Scenario B.

elevated \bar{T}^* .

2) *Increased Loading Capacity (Scenario B)*: As shown in Fig. 11, the short-term dynamic performances of both MPPT and reference operations are quite similar to the step-up responses of Scenario A in Fig. 9 and Fig. 10. Nevertheless, after a short-lived tracking of $P_{P2G,ref}$ at 800kW, the actual load P_{P2G} under reference operation is restricted to a maximum load of 721.7kW at approximately $t = 200$ s. The curve of I_{el} indicates that the upper limit $I'_{el,max}$ designed in the current control loop in Fig. 7 plays an active role in this process: the stabilized P_{fur} is not sufficient to ensure a stack-entrance temperature of T_{min} at the previous I_{el} ; thus, the current has to be restricted to $I'_{el,max}$, operating at the maximum production rate affordable by P_{fur} . This condition does not arise in the MPPT operation at state MPP₃ because a higher \bar{T}^* and a smaller π_{ca}^* have been selected to increase $I'_{el,max}$ calculated by (6).

In fact, a closer look at the steady-state model depicted in Fig. 6 indicates that the reference operation point is no longer within the feasible region (right-hand side of the 800kW FC) in Scenario B. Apart from improving efficiency, the other advantageous effect of the MPPT operation is revealed: the steady-state loading capacity of HT-P2G can be enhanced because of the utilization of parameter feasibilities.

C. Operation under Fluctuating Load Command

To characterize the implementation effects of the proposed MPPT strategy under fluctuating load command, we assume the occurrence of Scenario C, where the HT-P2G plant participates in automatic generation control (AGC) as a flexible load. Specifically, in this case, the plant receives an AGC setpoint for $P_{P2G,ref}$ every 4 seconds from the grid regulator based on modified PJM AGC data [26].

Based on the same profile of AGC signal $P_{P2G,ref}$, the plant operations under both MPPT and reference strategies are simulated for 1 hour as shown in Fig. 12. Rapid tracking of P_{P2G} to

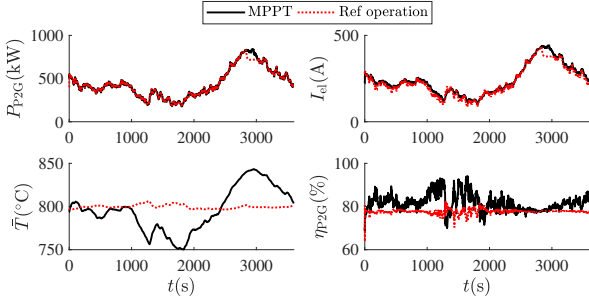


Fig. 12. The 1-hour operation of the HT-P2G system under a fluctuating AGC signal $P_{P2G,ref}$ (updated every 4 seconds): Scenario C.

TABLE III
PRODUCTIVE PERFORMANCE OF THE 1-HOUR OPERATION UNDER AGC

Operation strategy	Reference operation	MPPT operation
Hydrogen yield	8.656kg	9.084kg
Average efficiency	77.78%	80.87%

$P_{P2G,ref}$ can be observed under both strategies except for the several minutes at approximately $t = 2800s$ when $P_{P2G,ref}$ exceeds the load capacity of reference operation, and P_{P2G} is thus restricted to 721.7kW as in Scenario B. Moreover, the hydrogen production rate I_{el} and the conversion efficiency η_{P2G} under MPPT are higher than reference operation most of the time except for some temperature-ramping occasions as analyzed in Scenario A. In brief, the MPPT effects given in Section IV-B still apply.

As a natural result, a better productive performance can be achieved by MPPT relative to the reference operation under a common AGC profile, as elaborated in Table III with regard to this 1-hour case.

V. CONCLUSIONS

By optimizing temperature and feed flow parameters of a high-temperature power-to-gas (HT-P2G) system, a maximum production point tracking (MPPT) strategy is proposed to improve the hydrogen production under variable load command given by grid regulation and then tested on a comprehensive dynamic system model.

The numerical results suggest that the short-term transient process under MPPT operation contains three stages with increasing time scales, but the load disturbances due to varying mass flow or temperature in the latter two stages are well compensated by the fast current control, and the system is essentially stabilized externally by the end of Stage I. As a result, the MPPT-controlled plant shows a satisfying response speed for grid regulation even though the internal transition costs a few minutes. Moreover, the steady-state conversion efficiency and available loading capacity are both increased by the MPPT strategy. These long-term advantageous effects significantly improve the hydrogen production under specific hourly or daily loading profiles.

APPENDIX A

DERIVATIONS OF UNDERLINED VARIABLES

As mentioned in Section III-A, the underlined variables in (3)-(9) can be formulated as functions of $(I_{el}, \bar{T}, \boldsymbol{\pi})$. In this section, the elaborated derivations are presented.

According to Fig. 4, the steady-state electrolysis voltage \underline{U}_{el} is the sum of the reversible voltage, concentration overvoltage, activation overvoltage and ohmic overvoltage:

$$\underline{U}_{el}(I_{el}, \bar{T}, \boldsymbol{\pi}) = N_{cel} [U_{rev}(\bar{T}, \bar{\boldsymbol{p}}(\boldsymbol{\pi})) + U_{con}(i_{el}, \bar{T}, \bar{\boldsymbol{p}}(\boldsymbol{\pi})) + U_{act}(i_{el}, \bar{T}) + i_{el} \cdot ASR(\bar{T})] \quad (11)$$

where $U_{rev}(\bar{T}, \bar{\boldsymbol{p}})$, $U_{con}(i_{el}, \bar{T}, \bar{\boldsymbol{p}})$, $U_{act}(i_{el}, \bar{T})$ and $\bar{\boldsymbol{p}}(\boldsymbol{\pi})$ can be obtained from [2]. Note that i_{el} is proportional to I_{el} :

$$i_{el} = \frac{1}{N_{cha} L_x L_{y,cha}} \cdot I_{el}. \quad (12)$$

The steady-state power consumption of compressor \underline{P}_{com} can be simply derived from the compressor model in Fig. 5:

$$\underline{P}_{com}(I_{el}) = I_{el} \cdot \frac{RT_{com}}{2F\eta_{com}} \cdot \ln \frac{p_{com}}{p_{out}} \quad (13)$$

which is actually proportional to the compressed molar flow and the logarithm of the compression ratio.

According to the definition of feed factors π_{ca} and π_{an} as illustrated in Fig. 4, the feedstock mass flows w_{ca} and w_{an} can be expressed as functions of I_{el} and corresponding feed factor:

$$w_{ca} = I_{el} \cdot \frac{M_{H_2O} N_{cel}}{2F\omega_{H_2O,in}} \cdot \pi_{ca}, \quad (14)$$

$$w_{an} = I_{el} \cdot \frac{0.5M_{O_2} N_{cel}}{2F\omega_{O_2,in}} \cdot \pi_{an}. \quad (15)$$

With the help of (14) and (15), the energy sinks contributed to feedstock warming and prewarming, \underline{P}_{war} and $\underline{P}_{war,pre}$, can be formulated as follows:

$$\underline{P}_{war}(I_{el}, \bar{T}, \boldsymbol{\pi}) = \frac{I_{el} N_{cel}}{2F} \cdot (k_T \bar{T} - T_{in}) \cdot \left(\frac{M_{H_2O}}{\omega_{H_2O,in}} \pi_{ca} c_{ca,in} + \frac{0.5M_{O_2}}{\omega_{O_2,in}} \pi_{an} c_{an,in} \right), \quad (16)$$

$$\underline{P}_{war,pre}(I_{el}, \boldsymbol{\pi}) = \frac{I_{el} N_{cel}}{2F} \cdot \left((T_{in} - T_{amb}) \frac{0.5M_{O_2}}{\omega_{O_2,in}} \pi_{an} c_{an,in} + (T_{vap} - T_{amb}) \frac{M_{H_2O}}{\omega_{H_2O,in}} \pi_{ca} c_{ca(liq),in} + (T_{in} - T_{vap}) \frac{M_{H_2O}}{\omega_{H_2O,in}} \pi_{ca} c_{ca,in} \right). \quad (17)$$

The equations (16) and (17) are obtained from the heat-capacity-based calculations in the warming and prewarming models of Fig. 3.

As for \underline{P}_{rea} and \underline{P}_{vap} , their steady-state calculations are clearly depicted in Fig. 3:

$$\underline{P}_{rea}(I_{el}, \bar{T}) = I_{el} \cdot U_{th}(k_T \bar{T}) \cdot N_{cel}, \quad (18)$$

$$\underline{P}_{vap}(I_{el}) = I_{el} \cdot \frac{N_{cel}}{2F} \cdot h_{vap}. \quad (19)$$

Note that $U_{th}(k_T \bar{T})$ can be obtained from the temperature dependencies of the enthalpies of H_2O , H_2 and O_2 according to the definition of the thermo-neutral voltage U_{th} [9].

REFERENCES

- [1] S. Clegg and P. Mancarella, "Integrated modeling and assessment of the operational impact of power-to-gas (P2G) on electrical and gas transmission networks," *IEEE Trans. Sustain. Energy*, vol. 6, no. 4, pp. 1234–1244, Oct 2015.
- [2] F. Petipas, A. Brisse, and C. Bouallou, "Model-based behaviour of a high temperature electrolyser system operated at various loads," *Journal of Power Sources*, vol. 239, pp. 584–595, 2013.
- [3] M. Kopp, D. Coleman, C. Stiller, K. Scheffer, J. Aichinger, and B. Scheppat, "Energiepark mainz: Technical and economic analysis of the worldwide largest power-to-gas plant with pem electrolysis," *Int J Hydrogen Energy*, vol. 42, no. 19, pp. 13 311–13 320, 2017.
- [4] M. Frank, R. Deja, R. Peters, L. Blum, and D. Stolten, "Bypassing renewable variability with a reversible solid oxide cell plant," *Applied Energy*, vol. 217, pp. 101–112, 2018.
- [5] H. Khani and H. E. Z. Farag, "Optimal day-ahead scheduling of power-to-gas energy storage and gas load management in wholesale electricity and gas markets," *IEEE Trans. Sustain. Energy*, vol. PP, no. 99, pp. 1–1, 2017.
- [6] G. Gahleitner, "Hydrogen from renewable electricity: An international review of power-to-gas pilot plants for stationary applications," *Int J Hydrogen Energy*, vol. 38, no. 5, pp. 2039–2061, 2013.
- [7] M. Archambault, "Power-to-gas: Hydrogen energy storage to leverage infrastructure," http://emc-mec.ca/wp-content/uploads/TS1_3_POWER-TO-GAS_HYDROGEN-ENERGY-STORAGE-USING-RENEWABLES-TO-POWER-FUEL-CELL-ELECTRIC-VEHICLES.pdf, 2015.
- [8] J. Udagawa, P. Aguiar, and N. Brandon, "Hydrogen production through steam electrolysis: Model-based steady state performance of a cathode-supported intermediate temperature solid oxide electrolysis cell," *J Power Sources*, vol. 166, no. 1, pp. 127 – 136, 2007.
- [9] Z. Pan, Q. Liu, L. Zhang, J. Zhou, C. Zhang, and S. H. Chan, "Experimental and thermodynamic study on the performance of water electrolysis by solid oxide electrolyzer cells with Nb-doped Co-based perovskite anode," *Applied energy*, vol. 191, pp. 559–567, 2017.
- [10] P. Kazempoor and R. Braun, "Model validation and performance analysis of regenerative solid oxide cells: Electrolytic operation," *Int J Hydrogen Energy*, vol. 39, no. 6, pp. 2669 – 2684, 2014.
- [11] J. Padulles, G. Ault, and J. McDonald, "An integrated SOFC plant dynamic model for power systems simulation," *Journal of Power sources*, vol. 86, no. 1-2, pp. 495–500, 2000.
- [12] F. Gasser, "An analytical, control-oriented state space model for a PEM fuel cell system," *Ecole Polytechnique Federale de Lausanne, Lausanne*, 2006.
- [13] J. Milewski, A. Szczęśniak, and J. Lewandowski, "Dynamic characteristics of auxiliary equipment of SOFC/SOEC hydrogen peak power plant," *IERI Procedia*, vol. 9, pp. 82–87, 2014.
- [14] J. O'Brien, M. McKellar, E. Harvego, and C. Stoots, "High-temperature electrolysis for large-scale hydrogen and syngas production from nuclear energy—summary of system simulation and economic analyses," *Int J Hydrogen Energy*, vol. 35, no. 10, pp. 4808–4819, 2010.
- [15] L. Wang, M. Pérez-Fortes, H. Madi, S. Diethelm, F. Maréchal *et al.*, "Optimal design of solid-oxide electrolyzer based power-to-methane systems: A comprehensive comparison between steam electrolysis and co-electrolysis," *Applied Energy*, vol. 211, pp. 1060–1079, 2018.
- [16] Y. Luo, X.-y. Wu, Y. Shi, A. F. Ghoniem, and N. Cai, "Exergy analysis of an integrated solid oxide electrolysis cell-methanation reactor for renewable energy storage," *Applied Energy*, vol. 215, pp. 371–383, 2018.
- [17] X. Zhang, J. E. O'Brien, G. Tao, C. Zhou, and G. K. Housley, "Experimental design, operation, and results of a 4kW high temperature steam electrolysis experiment," *Journal of Power Sources*, vol. 297, pp. 90 – 97, 2015.
- [18] J. M. Corrêa, F. A. Farret, L. N. Canha, and M. G. Simoes, "An electrochemical-based fuel-cell model suitable for electrical engineering automation approach," *IEEE Trans. Ind. Electron.*, vol. 51, no. 5, pp. 1103–1112, 2004.
- [19] X. Xing, J. Lin, C. Wan, and Y. Song, "Modeling the dynamic electrical behavior of high temperature electrolysis for hydrogen production," in *2017 IEEE PESGM*, July 2017, pp. 1–5.
- [20] A. Kirubakaran, S. Jain, and R. Nema, "A review on fuel cell technologies and power electronic interface," *Renewable and Sustainable Energy Reviews*, vol. 13, no. 9, pp. 2430–2440, 2009.
- [21] H. Yu, J. Jia, G. Chen, and X. Chen, "Temperature control of electric furnace based on fuzzy pid," in *Electronics and Optoelectronics (ICEOE), 2011 International Conference on*, vol. 3. IEEE, 2011, pp. V3–41.
- [22] K. Meier, "Hydrogen production with sea water electrolysis using norwegian offshore wind energy potentials," *International Journal of Energy and Environmental Engineering*, vol. 5, no. 2-3, p. 104, 2014.
- [23] T. Zhao and Z. Ding, "Cooperative optimal control of battery energy storage system under wind uncertainties in a microgrid," *IEEE Trans. Power Syst.*, vol. 33, no. 2, pp. 2292–2300, 2018.
- [24] K. Clark, N. W. Miller, and J. J. Sanchez-Gasca, "Modeling of ge wind turbine-generators for grid studies," *GE Energy*, vol. 4, pp. 0885–8950, 2010.
- [25] A. Isaksson and S. Graebe, "Derivative filter is an integral part of PID design," *IEE Proceedings-Control Theory and Applications*, vol. 149, no. 1, pp. 41–45, 2002.
- [26] T. Chakraborty, D. Watson, and M. Rodgers, "Automatic generation control using an energy storage system in a wind park," *IEEE Trans. Power Syst.*, vol. 33, no. 1, pp. 198–205, Jan 2018.